

Pressure from dark matter annihilation and the rotation curve of spiral galaxies

M. Wechakama^{1★} and Y. Ascasibar^{2★}

¹*Astrophysikalisches Institut Potsdam, An der Sternwarte 16, Potsdam 14482, Germany*

²*Departamento de Física Teórica, Universidad Autónoma de Madrid, Madrid 28049, Spain*

Accepted 2010 December 31. Received 2010 December 10; in original form 2010 July 15

ABSTRACT

The rotation curves of spiral galaxies are one of the basic predictions of the cold dark matter paradigm, and their shape in the innermost regions has been hotly debated over the last decades. The present work shows that dark matter annihilation into electron–positron pairs may affect the observed rotation curve by a significant amount. We adopt a model-independent approach, where all the electrons and positrons are injected with the same initial energy $E_0 \sim m_{\text{dm}}c^2$ in the range from 1 MeV to 1 TeV and the injection rate is constrained by *INTEGRAL*, *Fermi* and *HESS* data. The pressure of the relativistic electron–positron gas is determined by solving the diffusion-loss equation, considering inverse Compton scattering, synchrotron radiation, Coulomb collisions, bremsstrahlung and ionization. For values of the gas density and magnetic field that are representative of the Milky Way, it is estimated that pressure gradients are strong enough to balance gravity in the central parts if $E_0 < 1$ GeV. The exact value depends somewhat on the astrophysical parameters, and it changes dramatically with the slope of the dark matter density profile. For very steep slopes, as those expected from adiabatic contraction, the rotation curves of spiral galaxies would be affected on $\sim \text{kpc}$ scales for most values of E_0 . By comparing the predicted rotation curves with observations of dwarf and low surface brightness galaxies, we show that the pressure from dark matter annihilation may improve the agreement between theory and observations in some cases, but it also imposes severe constraints on the model parameters (most notably, the inner slope of halo density profile, as well as the mass and the annihilation cross-section of dark matter particles into electron–positron pairs).

Key words: astroparticle physics – galaxies: haloes – galaxies: kinematics and dynamics – dark matter.

1 INTRODUCTION

Although cosmological observations are providing increasingly convincing evidence that non-baryonic cold dark matter (CDM) is the building block of structures in the Universe, the exact nature of dark matter remains a mystery. A promising approach to the problem relies on the possibility that dark matter particles annihilate into observable products such as photons, neutrinos, protons, antiprotons, electrons and positrons. Thus one can aim for indirect dark matter detection by looking for signatures of the annihilation products (see e.g. Bertone, Hooper & Silk 2005).

The most commonly studied signature is the emission of gamma-rays from the Galactic Centre (e.g. Bergström, Ullio & Buckley 1998; Baltz & Edsjö 1999; Gondolo & Silk 1999; Morselli et al.

2002; Ullio et al. 2002; Stoehr et al. 2003; Cesarini et al. 2004; Prada et al. 2004; Aharonian et al. 2006; Springel et al. 2008; Cirelli & Panci 2009; Fornasa et al. 2009; Bernal & Palomares-Ruiz 2010, among many others) as well as photons at other frequencies (e.g. Colafrancesco & Mele 2001; Regis 2008; Regis & Ullio 2008; Bergström et al. 2009; Cholis et al. 2009; Pato, Pieri & Bertone 2009; Crocker et al. 2010; Profumo & Ullio 2010). As the annihilation products travel through the surrounding medium, they heat and ionize the gas, potentially leaving an imprint on the cosmic microwave background (CMB; Chen & Kamionkowski 2004; Colafrancesco 2004; Padmanabhan & Finkbeiner 2005; Mapelli, Ferrara & Pierpaoli 2006; Zhang et al. 2006, 2007; Hooper, Finkbeiner & Dobler 2007; Cirelli, Iocco & Panci 2009; Cumberbatch et al. 2009; Galli et al. 2009; Kanzaki, Kawasaki & Nakayama 2010) and the H I 21 cm spectral line (Furlanetto, Oh & Pierpaoli 2006; Valdés et al. 2007; Chuzhoy 2008). Heating and ionization of the surrounding baryonic gas can also affect the

★E-mail: maneenate@aip.de (MW); yago.ascasibar@uam.es (YA)

formation of the first stars (Iocco et al. 2008; Spolyar, Freese & Gondolo 2008; Natarajan, Tan & O’Shea 2009; Ripamonti et al. 2010) and the formation and evolution of galaxies (Ascasibar 2007; Ripamonti, Mapelli & Ferrara 2007; Natarajan, Croton & Bertone 2008).

In this paper, we investigate the contribution of dark matter annihilation to the total gas pressure and consider the possibility that it has a significant effect on the rotation curve of spiral galaxies. While rotation curves provided one of the first and most important pieces of evidence for the existence of dark matter (see e.g. Sofue & Rubin 2001, and references therein), their shape in the inner regions of gas-rich dwarf and low surface brightness (LSB) spiral galaxies is one of the outstanding issues in modern cosmology (see e.g. de Blok 2010, for a recent discussion).

Observationally, rotation curves are found to rise approximately linearly with radius, consistent with a constant density core in the dark matter distribution (e.g. Flores & Primack 1994; Moore 1994; Burkert 1995; Kravtsov et al. 1998; Borriello & Salucci 2001; de Blok et al. 2001, 2008; de Blok & Bosma 2002; Marchesini et al. 2002; Donato, Gentile & Salucci 2004b; Gentile et al. 2004; Kuzio de Naray, McGaugh & de Blok 2008; Spano et al. 2008; Oh et al. 2010a) rather than the steep power law predicted by cosmological N -body simulations (e.g. Dubinski & Carlberg 1991; Navarro, Frenk & White 1996, 1997; Fukushige & Makino 1997, 2001; Ghigna et al. 1998, 2000; Moore et al. 1998, 1999; Jing & Suto 2000; Klypin et al. 2001; Power et al. 2003; Ascasibar et al. 2004; Fukushige, Kawai & Makino 2004; Hayashi et al. 2004; Navarro et al. 2004, 2010; Diemand et al. 2005, 2008; Reed et al. 2005; Ascasibar & Gottlöber 2008; Gao et al. 2008). Several modifications to the standard CDM scenario, such as warm (Colín, Avila-Reese & Valenzuela 2000; Sommer-Larsen & Dolgov 2001), repulsive (Goodman 2000), fluid (Peebles 2000), fuzzy (Hu, Barkana & Gruzinov 2000), decaying (Cen 2001), annihilating (Kaplinghat, Knox & Turner 2000) or self-interacting (Spergel & Steinhardt 2000; Yoshida et al. 2000; Davé et al. 2001) dark matter, and even alternative theories of gravitation (e.g. McGaugh & de Blok 1998; Sanders & McGaugh 2002; Gentile, Famaey & de Blok 2011) have been proposed in order to explain the discrepancy.

Here we focus on the energy density associated to electrons and positrons arising from dark matter annihilations, neglecting other processes, such as dark matter decay, or other annihilation products, such as protons and antiprotons (whose contribution is severely constrained by recent observational data; see e.g. Adriani et al. 2009b). We adopt a model-independent approach, in which all particles are created with the same initial energy $E_0 \sim m_{\text{dm}} c^2$. Results for a particular dark matter candidate can be obtained by convolution with the appropriate source function.

Since the characteristic energies involved are of the order of the mass of the dark matter particle, and this mass is usually much larger than the rest mass of the electron, electrons and positrons will be relativistic at the moment of their creation. However, they can efficiently lose their energy through different processes, such as inverse Compton scattering (ICS), synchrotron radiation, Coulomb collisions, bremsstrahlung and ionization. Throughout this paper, we will often use the Lorentz factor γ to express the energy $E = \gamma m_e c^2$, where m_e denotes the rest mass of electron, and c is the speed of light.

The pressure associated to these particles, hereafter referred to as ‘dark matter pressure,’ is given by

$$P_{\text{dm}}(r) = \frac{m_e c^2}{3} \int_1^\infty \frac{dn}{d\gamma}(r, \gamma) \left(\frac{\gamma^2 - 1}{\gamma} \right) d\gamma, \quad (1)$$

where the electron–positron spectrum $(dn/d\gamma)(r, \gamma)$ is the number density of particles with Lorentz factor γ at a radius r from the centre of the dark matter halo. The pressure gradient induces an acceleration

$$a_{\text{dm}}(r) = -\frac{1}{\rho_g(r)} \frac{dP_{\text{dm}}(r)}{dr}, \quad (2)$$

where $\rho_g(r)$ is the gas density at radius r , that opposes the gravitational pull towards the centre, affecting observable quantities such as the circular velocity

$$v_c(r) = \sqrt{\frac{GM(r)}{r} + \frac{r}{\rho_g(r)} \frac{dP_{\text{dm}}(r)}{dr}}. \quad (3)$$

It is our aim to show that, depending on the model parameters, the contribution of dark matter pressure to the rotation curve may not be negligible. Section 2 describes the procedure followed to estimate the electron–positron spectrum. The ensuing dark matter pressure is presented in Section 3, and the role of each astrophysical parameter (gas density and ionization fraction of the interstellar medium (ISM), intensity of the magnetic field and dark matter density profile) is discussed in detail. The effect on the rotation curve is investigated in Section 4, and our main conclusions are briefly summarized in Section 5.

2 THE ELECTRON–POSITRON SPECTRUM

2.1 Propagation

The propagation of electrons and positrons through the ISM is determined by the diffusion-loss equation

$$\begin{aligned} \frac{\partial}{\partial t} \frac{dn}{d\gamma}(\mathbf{x}, \gamma) = & \nabla \cdot \left[K(\mathbf{x}, \gamma) \nabla \frac{dn}{d\gamma}(\mathbf{x}, \gamma) \right] \\ & + \frac{\partial}{\partial \gamma} \left[b(\mathbf{x}, \gamma) \frac{dn}{d\gamma}(\mathbf{x}, \gamma) \right] \\ & + Q(\mathbf{x}, \gamma). \end{aligned} \quad (4)$$

We assume a diffusion coefficient of the form

$$K(\gamma) = K_0 \gamma^\delta \quad (5)$$

with $K_0 = 1.67 \times 10^{25} \text{ cm}^2 \text{ s}^{-1}$ and $\delta = 0.7$, independent of Galactic location (MED model in Donato et al. 2004a). The energy loss rate

$$b(\mathbf{x}, \gamma) \equiv -\frac{d\gamma}{dt}(\mathbf{x}, \gamma) = \sum_i b_i(\mathbf{x}, \gamma) \quad (6)$$

is a sum over the relevant physical processes, and the source term $Q(\mathbf{x}, \gamma)$ represents the instantaneous electron–positron injection rate.

Given enough time, the electron–positron population will approach a steady-state distribution, $(\partial/\partial t)(dn/d\gamma)(\mathbf{x}, \gamma) = 0$. Assuming that $b(\mathbf{x}, \gamma)$ varies smoothly in space, the particle spectrum fulfils the relation

$$\frac{\partial y(\mathbf{x}, \gamma)}{\partial \gamma} + \frac{K(\gamma)}{b(\gamma)} \nabla^2 y(\mathbf{x}, \gamma) = -Q(\mathbf{x}, \gamma), \quad (7)$$

where

$$y(\mathbf{x}, \gamma) \equiv b(\gamma) \frac{dn}{d\gamma}(\mathbf{x}, \gamma). \quad (8)$$

Imposing $(dn/d\gamma)(\mathbf{x}, \gamma) = 0$ at infinity, one obtains the Green’s function

$$G(\mathbf{x}, \gamma, \mathbf{x}_s, \gamma_s) = \frac{\exp[-(|\mathbf{x} - \mathbf{x}_s|^2)/(2\Delta\lambda^2)]}{(2\pi\Delta\lambda^2)^{3/2}} \Theta(\gamma - \gamma_s) \quad (9)$$

and either the image charges method or an expansion over the eigenfunctions of the linear differential operator may be used to derive the Green's function for other boundary conditions (see e.g. Baltz & Edsjö 1999; Delahaye et al. 2009). The electron–positron spectrum is given by

$$\frac{dn}{d\gamma}(\mathbf{x}, \gamma) = \frac{1}{b(\mathbf{x}, \gamma)} \times \int_{\gamma}^{\infty} d\gamma_s \int_0^{\infty} d^3\mathbf{x}_s \frac{\exp[-(|\mathbf{x} - \mathbf{x}_s|^2)/(2\Delta\lambda^2)]}{(2\pi\Delta\lambda^2)^{3/2}} Q(\mathbf{x}_s, \gamma_s), \quad (10)$$

where the quantity

$$\Delta\lambda^2 = \lambda^2(\gamma) - \lambda^2(\gamma_s) \quad (11)$$

is related to the characteristic diffusion length of the electrons and positrons, and γ_s denotes their initial energy. The variable λ is defined as

$$\lambda^2(\gamma) = \int_{\gamma}^{\infty} \frac{2K(\gamma)}{b(\gamma)} d\gamma. \quad (12)$$

Considering the dark matter halo as an spherically symmetric source, the spatial integral can be reduced to one dimension, and the electron–positron spectrum is finally given by the expression

$$\begin{aligned} \frac{dn}{d\gamma}(r, \gamma) &= \frac{1}{b(\gamma)} \frac{\exp[-(r^2)/(2\Delta\lambda^2)]}{(2\pi r^2 \Delta\lambda^2)^{1/2}} \\ &\times \left\{ \int_{\gamma}^{\infty} d\gamma_s \int_0^{\infty} dr_s r_s \exp\left(-\frac{r_s^2}{2\Delta\lambda^2}\right) \right. \\ &\times \left. \left[\exp\left(\frac{rr_s}{\Delta\lambda^2}\right) - \exp\left(-\frac{rr_s}{\Delta\lambda^2}\right) \right] Q(r_s, \gamma_s) \right\}. \quad (13) \end{aligned}$$

2.2 Loss rates

Electrons and positrons can lose their energy by several physical processes as they move through the ISM. We consider ICS of CMB and starlight photons, synchrotron radiation, Coulomb collisions, bremsstrahlung and ionization of neutral hydrogen atoms.

The energy loss rates depend on the energy of the particle. High-energy electrons and positrons mainly lose energy by ICS (e.g. Sarazin 1999). The relevant loss function is

$$b_{\text{ICS}}(\gamma) = \frac{4}{3} \frac{\sigma_T}{m_e c} \gamma^2 U_{\text{rad}}, \quad (14)$$

where σ_T is the Thomson cross-section and

$$U_{\text{rad}} = U_{\text{CMB}} + U_{\text{stars}} + U_{\text{dust}} \approx 0.9 \text{ eV cm}^{-3} \quad (15)$$

is the combined radiation energy density of the CMB, starlight and thermal dust emission (see e.g. Porter & Moskalenko 2005).

Synchrotron radiation is another important loss mechanism at high energies. The expression for the loss rate is similar to that of ICS, substituting the radiation energy density in equation (14) by the energy density of the magnetic field, $U_B = B^2/(8\pi)$, where B is the intensity of the magnetic field:

$$b_{\text{syn}}(\gamma) = \frac{4}{3} \frac{\sigma_T}{m_e c} \gamma^2 U_B. \quad (16)$$

For lower energy electrons and positrons, Coulomb interactions with the thermal plasma must be taken into account. The loss rate is approximately (Rephaeli 1979)

$$b_{\text{Coul}}(\gamma) \approx 1.2 \times 10^{-12} n_e \left[1 + \frac{\ln(\gamma/n_e)}{75} \right] \text{ s}^{-1}, \quad (17)$$

where n_e is the number density of thermal electrons.

Collisions with thermal ions and electrons also produce radiation through bremsstrahlung. The loss rate due to bremsstrahlung can be approximated as (Blumenthal & Gould 1970)

$$b_{\text{brem}}(\gamma) \approx 1.51 \times 10^{-16} n_e \gamma [\ln(\gamma) + 0.36] \text{ s}^{-1}. \quad (18)$$

Additional energy losses come from the ionization of hydrogen atoms. The loss rate is given in Longair (1981):

$$\begin{aligned} b_{\text{ion}}(\gamma) &= \frac{q_e^4 n_H}{8\pi\epsilon_0^2 m_e^2 c^3 \sqrt{1 - (1/\gamma^2)}} \left[\ln \frac{\gamma(\gamma^2 - 1)}{2(I/m_e c^2)^2} \right. \\ &\quad \left. - \left(\frac{2}{\gamma} - \frac{1}{\gamma^2} \right) \ln 2 + \frac{1}{\gamma^2} + \frac{1}{8} \left(1 - \frac{1}{\gamma} \right)^2 \right], \quad (19) \end{aligned}$$

where n_H is the number density of hydrogen atoms, q_e is the charge of electron, ϵ_0 is the permittivity of free space and I is the ionization energy of the hydrogen atom. The number density of thermal electrons and neutral atoms can be expressed in terms of the total ISM gas density ρ_g and the ionization fraction X_{ion} as

$$n_e = \frac{\rho_g}{m_p} X_{\text{ion}} \quad (20)$$

and

$$n_H = \frac{\rho_g}{m_p} (1 - X_{\text{ion}}), \quad (21)$$

respectively.

2.3 Source term

Since the electrons and positrons in our model originate from the annihilation of dark matter particles, the production rate is dictated by the dark matter number density and the annihilation rate into electron–positron pairs:

$$Q(r, \gamma) = n_{\text{dm}}(r) n_{\text{dm}^*}(r) \langle \sigma v \rangle_{e^\pm} \frac{dN_{e^\pm}}{d\gamma}, \quad (22)$$

where n_{dm} and n_{dm^*} denote the number densities of dark matter particles and antiparticles, respectively, $\langle \sigma v \rangle_{e^\pm}$ is the thermal average of the annihilation cross-section times the dark matter relative velocity and $dN_{e^\pm}/d\gamma$ is the injection spectrum of electrons and positrons in the final state.

Assuming all electrons and positrons are injected with the same energy $\gamma_0 \sim m_{\text{dm}}/m_e$:

$$Q(r, \gamma) = Q_0(r) \delta(\gamma - \gamma_0), \quad (23)$$

where

$$Q_0(r) = 2 \left[\frac{\rho_{\text{dm}}(r)}{m_{\text{dm}}} \right]^2 \langle \sigma v \rangle_{e^\pm} \quad (24)$$

is the local production rate per unit volume per unit time and $\delta(\gamma - \gamma_0)$ denotes a Dirac delta function.

Although this is a rather coarse approximation, it has the advantage of being absolutely model independent. Moreover, the contribution of electrons and positrons to the gas pressure will be mostly determined by their total number and average initial energy, with the details of the injection spectrum playing only a minor role. The factor of 2 in equation (24) accounts for one electron and one positron produced per annihilation event, and self-conjugate dark matter particles have been assumed. If dark matter particles and antiparticles were different, $n_{\text{dm}} = n_{\text{dm}^*} = \rho_{\text{dm}}(r)/(2m_{\text{dm}})$ and Q_0 would decrease by a factor of 4. For the dark matter density $\rho_{\text{dm}}(r)$, we consider a perfectly spherically symmetric halo described by a

density profile of the form

$$\rho_{\text{dm}}(r) = \frac{\rho_s}{(r/r_s)^\alpha [1 + (r/r_s)]^{3-\alpha}}, \quad (25)$$

where r_s and ρ_s denote a characteristic density and radius of the halo, respectively, and the α is the inner logarithmic slope of the density profile. Local inhomogeneities that would boost the expected signal, such as small-scale clumpiness or the presence of subhaloes, are not taken into account. The shape of the dark matter density profile in the inner regions is far from being a settled question. As stated in the introduction, N -body simulations suggest that, at least in the absence of baryons, the profile should be quite steep near the centre ($\alpha \sim 1$), in apparent contradiction with observations. Traditionally, it has been argued that the presence of gas and stars makes the profile even steeper due to the effects of adiabatic contraction (Blumenthal et al. 1986), although some recent claims have also been made in the opposite direction (e.g. El-Zant, Shlosman & Hoffman 2001; Mashchenko, Couchman & Wadsley 2006; Oh et al. 2010b). Given the current uncertainties, we have left the inner slope of the density profile as a free parameter of the model.

For similar reasons, we also consider the injection energy as a free parameter and investigate values of the initial Lorentz factor γ_0 between 2 and 2×10^6 , corresponding to energies $E_0 = \gamma_0 m_e c^2$ from about 1 MeV to 1 TeV. The production rate Q_0 , on the other hand, is strongly constrained by different Galactic observations. At high energies, we consider observations of the electron–positron spectrum in the solar neighbourhood by *HESS* and the Large Area Telescope (LAT) onboard the *Fermi* satellite (Aharonian et al. 2008; Abdo et al. 2009). More specifically, the predicted amount of electrons and positrons cannot exceed the observed values for *any* Lorentz factor γ . Given the energy dependence of the observed spectrum, $[dn/dE]_{\text{obs}} \sim E^{-3}$, and the energy losses, $b(E) \sim E^2$, the most restrictive constraint comes from the spectrum near the injection energy, where propagation can be safely neglected and $[dn/dE]_{\text{model}} \approx (Q_0/b) \propto E^{-2}$. The maximum production rate allowed by the data can then be expressed as

$$Q_0(r_\odot) < b(\gamma_0) \left[\frac{dn}{dE} \right]_{\text{obs}} (\gamma_0). \quad (26)$$

Another, completely independent upper limit, valid at all energies, can be obtained from the observed intensity of the 511-keV line that measures the positron annihilation rate at the Galactic Centre. In order to fully explain the line with dark matter annihilations, it is necessary that (Ascasibar et al. 2006)

$$\frac{\langle \sigma v \rangle_{511}}{2.6 \times 10^{-30} \text{ cm}^3 \text{ s}^{-1}} = \left(\frac{m_{\text{dm}} c^2}{1 \text{ MeV}} \right)^2, \quad (27)$$

so one just have

$$Q_0(r_\odot) < 2 \left[\frac{\rho_{\text{dm}}(r_\odot)}{m_{\text{dm}}} \right]^2 \langle \sigma v \rangle_{511} \quad (28)$$

in order not to overproduce the observed signal.

The corresponding exclusion regions are shown in Fig. 1, together with the production rates used in our calculation at the position of the Sun, $r_\odot = 8.5$ kpc. These conditions constitute strict upper limits, since astrophysical sources will also contribute to the relativistic particle budget, but the annihilation cross-sections they imply are comparable to or larger than the ones required to explain the cosmic dark matter density:

$$\Omega_{\text{dm}} \sim \frac{10^{-26} \text{ cm}^3 \text{ s}^{-1}}{\langle \sigma v \rangle_{e^\pm}}. \quad (29)$$

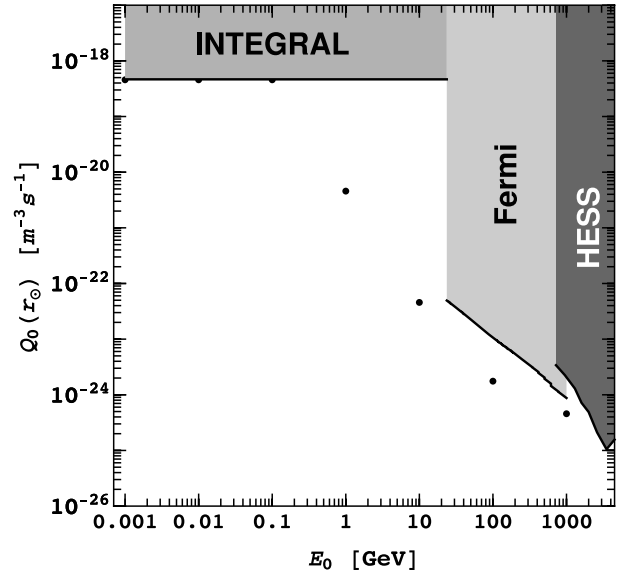


Figure 1. Exclusion regions and production rates at the position of the Sun: black dots are the adopted values of the instantaneous production rate Q_0 (see Table 1). Shaded regions above the black lines are excluded by *INTEGRAL*, *Fermi* and *HESS* data.

Table 1. Initial Lorentz factors, energies, cross-sections and production rates at the position of the Sun used in our calculations.

γ_0	E_0 (GeV)	$\langle \sigma v \rangle_{e^\pm}$ ($\text{cm}^3 \text{ s}^{-1}$)	$Q_0(r_\odot)$ ($\text{m}^{-3} \text{ s}^{-1}$)
2×10^0	1.022×10^{-3}	2.6×10^{-30}	4.7×10^{-19}
2×10^1	1.022×10^{-2}	2.6×10^{-28}	4.7×10^{-19}
2×10^2	1.022×10^{-1}	2.6×10^{-26}	4.7×10^{-19}
2×10^3	1.022×10^0	2.6×10^{-26}	4.7×10^{-21}
2×10^4	1.022×10^1	2.6×10^{-26}	4.7×10^{-23}
2×10^5	1.022×10^2	1.0×10^{-25}	1.8×10^{-24}
2×10^6	1.022×10^3	2.6×10^{-24}	4.7×10^{-25}

Therefore, we have set the injection rate according to equation (28) for $m_{\text{dm}} c^2 \leq 100$ MeV, while a cross-section compatible with the relic density constraint, $\langle \sigma v \rangle_{e^\pm} = 2.6 \times 10^{-26} \text{ cm}^3 \text{ s}^{-1}$, has been assumed for $100 \text{ MeV} \leq m_{\text{dm}} c^2 \leq 10 \text{ GeV}$, and slightly larger values (based on the positron excess observed by *PAMELA*; Adriani et al. 2009a) have been used for $m_{\text{dm}} c^2 \approx 100 \text{ GeV}$ and 1 TeV. Numeric values are given in Table 1.

3 DARK MATTER PRESSURE

Apart from the initial energy and injection rate of the electron–positron pairs, related to the nature of the dark matter particle, there are many astrophysical parameters that determine the contribution of dark matter annihilation to the total gas pressure. We will first define a canonical model based on observations of the Milky Way and then investigate the effect of each individual component by varying the values of the adopted parameters one by one. In all cases, we calculate the electron–positron spectrum as described in the previous section, and then estimate the dark matter pressure according to expression (1).

3.1 Canonical Milky Way model

Our canonical model assumes a dark matter density profile with $\alpha = 1$ (Navarro et al. 1997), $r_s = 17$ kpc and $\rho_s = 6 \times 10^{-22}$ kg m $^{-3}$, consistent with dynamical models of the Milky Way (e.g. Dehnen & Binney 1998; Klypin, Zhao & Somerville 2002). The virial mass of the Galaxy is thus $10^{12} M_\odot$, and the local dark matter density is $\rho_{\text{dm}}(r_\odot) c^2 = 0.3$ GeV cm $^{-3}$. The ISM is mainly composed by neutral hydrogen atoms ($X_{\text{ion}} = 0$) with number density $\rho_g/m_p \sim 1$ cm $^{-3}$ (Dehnen & Binney 1998; Ferrière 2001; Robin et al. 2003), and it is permeated by a uniform, tangled magnetic field whose intensity is $B \sim 6$ μ G throughout the Galaxy (Beck 2001; Ferrière 2001; Ascasibar & Díaz 2010).

The contribution of the individual loss terms described in Section 2.2 is plotted on the top panel in Fig. 2 for a model similar to the canonical one, but with $X_{\text{ion}} = 0.5$ (in order to have a non-zero contribution from Coulomb collisions and bremsstrahlung). ICS and synchrotron emission, being proportional to γ^2 , dominate at high energies, $\gamma > 10^4$. Bremsstrahlung is important in the intermediate range $10^3 < \gamma < 10^4$, and Coulomb collisions and ionization, roughly independent on γ , dominate at low energies, $\gamma < 10^3$. The time taken by the electron–positron population to reach equilibrium is of the same order as the time

$$t_{\text{rest}}(\gamma_0) = \int_1^{\gamma_0} \frac{1}{b(\gamma)} d\gamma, \quad (30)$$

that the particles take to loose all their energy, shown on the middle panel in Fig. 2 as a function of γ_0 . Although this time may be larger than the orbital time at $r \sim 500$ pc ($T \sim 10$ Myr, assuming $v \sim 220$ km s $^{-1}$) for $m_{\text{dm}} > 100$ MeV, a steady state will be reached as long as the conditions (dark matter and gas densities, magnetic field, etc.) evolve on time-scales longer than ~ 100 Myr, which is relatively short in astrophysical terms.

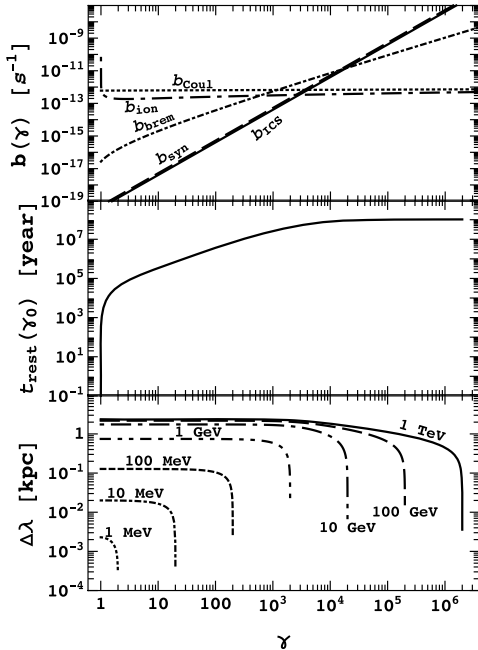


Figure 2. Energy losses, equilibrium time scales and characteristic diffusion lengths of electrons and positrons for $\rho_g/m_p = 1$ cm $^{-3}$, $B = 6$ μ G and $X_{\text{ion}} = 0.5$. On the top panel, Coulomb collisions, ionization, bremsstrahlung, synchrotron radiation and ICS are represented by dotted, dot-long dashed, dot-short dashed, dashed and solid lines, respectively.

The steady-state electron–positron spectrum at the position of the Sun, $r_\odot = 8.5$ kpc, is shown on the left-hand panel in Fig. 3 for different values of the initial energy E_0 . As stated above, all of the electrons and positrons are generated with the same γ_0 , according to Table 1. Propagation through the Galaxy and energy losses are accounted for by equation (13). The shape of the resulting spectrum is determined by the value of γ_0 , the production rate $Q_0(r)$, the loss rates $b(\gamma)$ implied by the values of ρ_g , B and X_{ion} and the diffusion coefficient $K(\gamma)$. Nevertheless, some insight may be gained by neglecting diffusion. For $K_0 = 0$,

$$\frac{dn}{d\gamma}(r_\odot, \gamma) = \frac{Q_0(r_\odot)}{b(\gamma)}; \quad (31)$$

the electron–positron spectrum is almost flat when ionization dominates the energy losses, and there is a transition at $\gamma \sim 10^3$ ($E \sim 1$ GeV) to the ICS–synchrotron regime, where $(dn/d\gamma) \propto \gamma^{-2}$. For low injection energies (1 to 100 MeV), the normalizations of the spectra are identical because the value of Q_0 is only constrained by the *INTEGRAL* data, whereas other constraints impose lower values at higher energies (see Fig. 1). In all cases, the spectra are cut at the injection energy γ_0 since no acceleration mechanism is included in our model.

The electron–positron spectrum closer to the centre of the Galaxy ($r = 10$ pc) is shown on the right-hand panel in Fig. 3. In general terms, the overall normalizations are higher than at the position of the Sun because of the higher dark matter density, and there is a sharp spectral feature near E_0 . The characteristic diffusion scale $\Delta\lambda$ plays an important role in both cases. As can be seen on the bottom panel of Fig. 2, $\Delta\lambda$ depends on the Lorentz factor of the electrons and positrons. It is zero at the injection value, and it rapidly increases for lower energies until it saturates at a maximum value that depends on E_0 . The spectrum at a given γ probes the effective value of the production rate $Q(r)$, averaged over the diffusion scale. This is not very relevant at the position of the Sun because the dark matter density does not vary much on kpc scales, but it becomes more important as one moves towards the central density cusp. For $\gamma \ll \gamma_0$, $\Delta\lambda$, and thus the effective production rate, is independent on γ . The larger E_0 , the larger the smoothing scale, and therefore the smaller the average density and the contrast with respect to the normalization at 8.5 kpc. As long as $\Delta\lambda$ is constant, the shape of the spectrum remains the same, flat for low Lorentz factors and proportional to γ^{-2} in the inverse Compton regime. Near the injection energy, $\Delta\lambda$ becomes very small, the effective production rate approaches the local source term $Q_0(r)$, much higher than the smoothed value, and the spectrum rises steeply just before the cut-off.

Finally, the contribution of dark matter annihilations to the gas pressure at a given radius can be obtained by substituting the electron–positron spectrum in equation (1). Results for different values of γ_0 compared with gas and magnetic pressure in the galaxy are presented in Fig. 4, compared to the thermal pressure of the gas $P_{\text{gas}} = nkT$ (where $n = \rho_g/m_p = 1$ cm $^{-3}$ is the gas density, k is the Boltzmann constant, and we have assumed a temperature $T = 100$ K, appropriate for the neutral gas in the Galactic disc and the magnetic pressure $P_{\text{mag}} = B^2/8\pi$, with $B = 6$ μ G).

For low injection energies, the pressure decreases sharply with distance from the Galactic Centre. For $E_0 > 1$ GeV, diffusion keeps the electron–positron spectrum (and the ensuing pressure) roughly constant within a radius of a few kpc. The highest values of the dark matter pressure are found for an initial energy $E_0 = 100$ MeV. Although the spectrum for $E_0 = 1$ and 10 MeV is similar (approximately constant up to the cut-off at γ_0 , because it dominated by

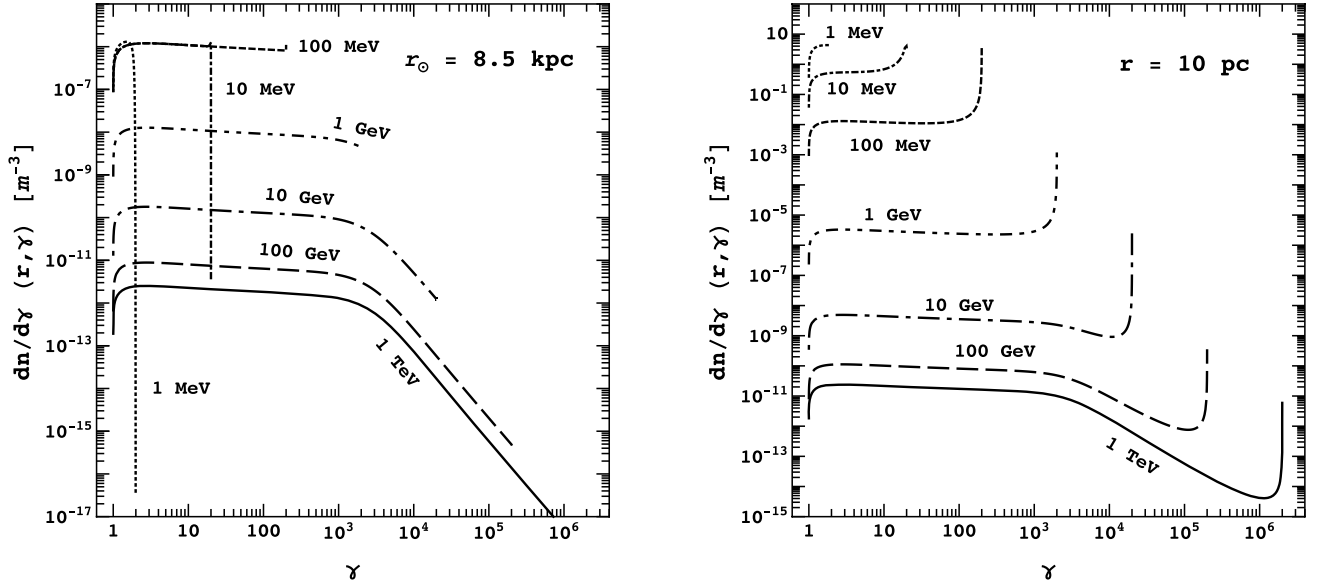


Figure 3. Electron–positron spectrum at the position of the Sun (left) and at $r = 10 \text{ pc}$ (right) for our canonical model of the Milky Way and different values of the injection energy E_0 .

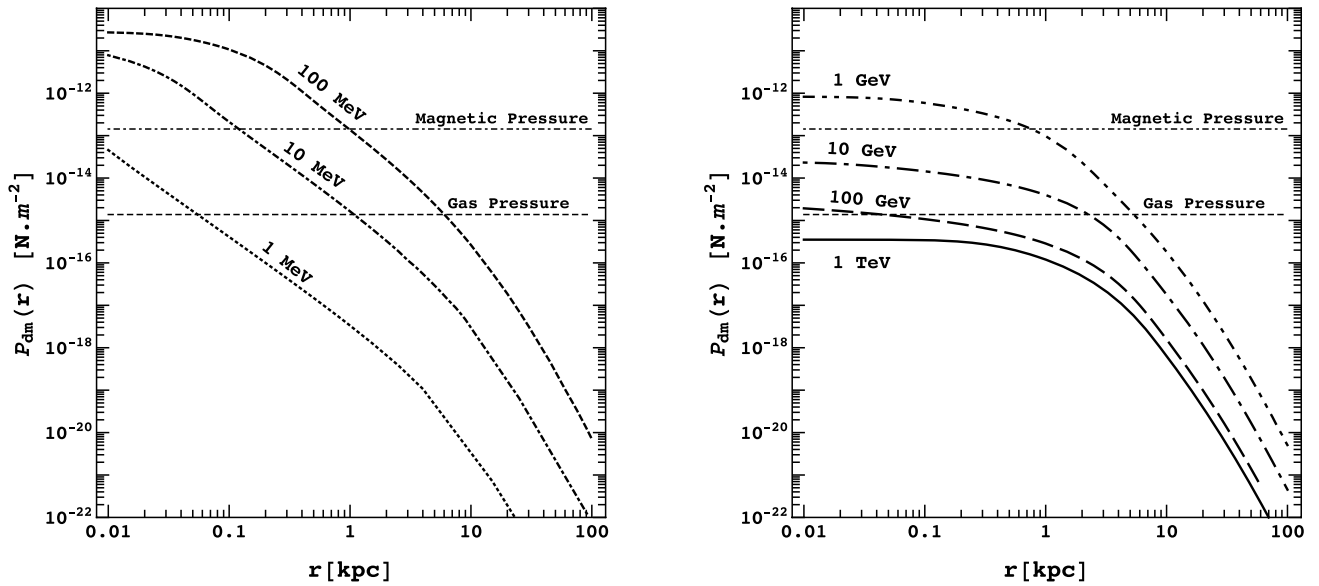


Figure 4. Dark matter pressure as a function of radius in our canonical model compared with gas and magnetic pressure.

ionization losses) and even has a higher normalization near the centre, the smaller upper limit of the integral in equation (1) yields significantly lower pressures. At high ($E_0 \geq 1 \text{ GeV}$) injection energies, the dark matter pressure is also lower, due to the smaller number density of dark matter particles. Most of the dark matter pressure for an initial energy E_0 , except $E_0 = 1 \text{ TeV}$, are higher than the pressure from the gas in the galaxy and for $E_0 = 10 \text{ MeV} - 1 \text{ GeV}$, the dark matter pressure is significantly higher than the pressure from magnetic fields.

3.2 Astrophysical parameters

We will now discuss the effect of the various astrophysical parameters that enter our calculation of the dark matter pressure, namely the intensity of the magnetic field, the density and ionization frac-

tion of the ISM gas and the inner slope of the dark matter density profile. As we did for the canonical model, we will compare the results obtained for different initial energies E_0 from $\sim 1 \text{ MeV}$ to 1 TeV and vary each of the astrophysical parameters in turn in order to assess how much they influence the results.

Magnetic fields affect the high-energy ($\gamma > 10^3$) tail of the electron–positron spectrum by setting the energy losses due to synchrotron radiation. As can be seen in Fig. 2, in our canonical model with $B = 6 \mu\text{G}$, the synchrotron term (16) is responsible for about 50 per cent of the energy loss at high energies, with ICS being responsible for most of the other 50 per cent. At low energies, energy losses are dominated by ionization of neutral hydrogen, and the contribution of synchrotron emission is negligible. The effect of varying B from 1 to $10 \mu\text{G}$ is plotted on the left-hand panel in Fig. 5. Not surprisingly, the results for an initial energy $E_0 < 1 \text{ GeV}$ are largely

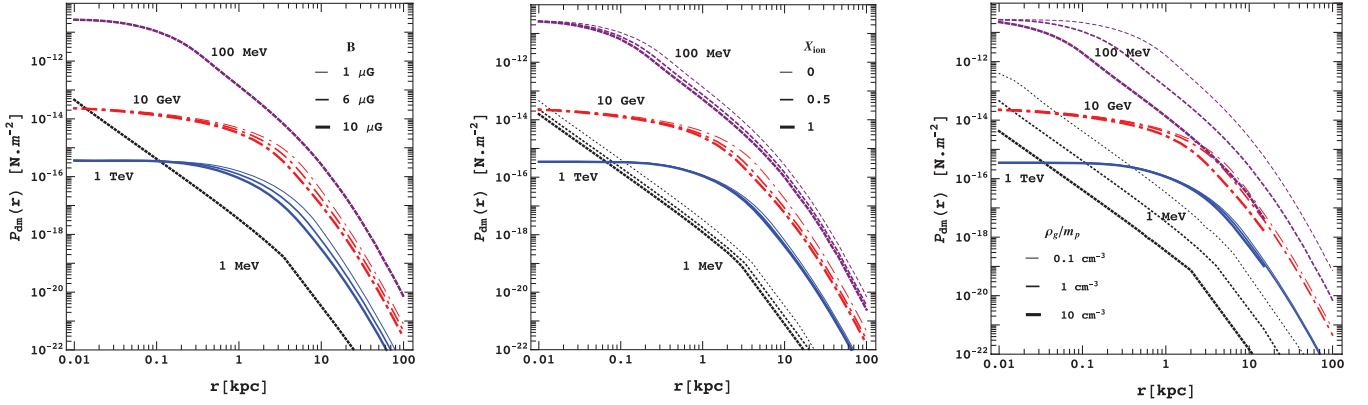


Figure 5. Effect of varying the magnetic field intensity from 1 to 10 μG (left), the ionization fraction X_{ion} from 0 to 1 (centre) and the ISM gas density from $\rho_g/m_p = 0.1$ to 10 cm^{-3} (right). The pressure profiles for $E_0 = 1 \text{ MeV}$, 100 MeV, 10 GeV and 1 TeV are represented by dotted, dashed, dot–dashed and solid lines, respectively.

unaffected. At higher energies, the pressure at large radii decreases with the magnetic field intensity because of the more rapid energy losses. However, the diffusion length becomes shorter, increasing the effective production rate and yielding a larger pressure near the centre of the Galaxy.

As explained in Section 2.2, the density of the ISM gas and the ionization fraction X_{ion} regulate the energy losses by Coulomb interactions, bremsstrahlung and ionization. For $X_{\text{ion}} = 0$ (our canonical model), the ISM gas is entirely composed of neutral hydrogen atoms, and the energy loss of the electrons and positrons with $\gamma < 10^3$ is dominated by the ionization process. At the other extreme, $X_{\text{ion}} = 1$, the ISM is already fully ionized, and the relevant energy losses are Coulomb collisions and bremsstrahlung. Since the total loss by these processes is higher than the loss by ionization, the maximum pressure happens when $X_{\text{ion}} = 0$ (middle panel of Fig. 5). The effect of changing the gas density from 0.1 to 10 cm^{-3} is shown on the right-hand panel. Higher densities yield lower dark matter pressures, simply because the energy losses are faster.

Finally, we calculate the dependence of dark matter pressure on the inner logarithmic slope α of the dark matter density profile. When varying α , we also modify the characteristic density and radius in expression (25) so that the dark matter density at the solar radius is equal to 0.3 GeV cm^{-3} and the virial mass of the Galaxy is $10^{12} M_\odot$. The appropriate values of ρ_s and r_s are quoted in Table 2 for several values of the inner slope. For $\alpha \geq 1.5$, the production rate Q_0 in equation (24) diverges rapidly at $r = 0$, so we add a cut-off based on the local annihilation rate $\Gamma(r)$:

$$Q_0(r) = 2 \left[\frac{\rho_{\text{dm}}(r) \exp[-t_0 \Gamma(r)]}{m_{\text{dm}}} \right]^2 \langle \sigma v \rangle_{e^\pm}, \quad (32)$$

Table 2. Characteristic density and radius of the dark matter density profile (equation 25) as a function of its asymptotic logarithmic inner slope α .

α	$\rho_s c^2 \text{ (GeV cm}^{-3}\text{)}$	$r_s \text{ (kpc)}$
1.0	0.3483	16.68
1.2	0.1975	20.34
1.4	0.09946	25.88
1.5	0.06658	29.81
1.7	0.02469	42.46
1.9	0.00615	70.30

where $t_0 = 13.7 \text{ Gyr}$ is the age of the Universe and $\Gamma(r) = [\rho_{\text{dm}}(r)/m_{\text{dm}}] \langle \sigma v \rangle_{e^\pm}$.

The dark matter pressure profiles obtained for $\alpha = 1, 1.2, 1.4, 1.5, 1.7$ and 1.9 are compared in Fig. 6. Since the central dark matter density increases dramatically with the value of the inner logarithmic slope, this is, by far, the most relevant astrophysical parameter, only second in importance to the injection energy E_0 related to the mass (and the precise nature) of the dark matter particle.

4 ROTATION CURVES

The gradient of the dark matter pressure induces an acceleration on the baryonic component that opposes the gravitational force. This acceleration, given by expression (2), is plotted in Fig. 7 for all the injection energies considered in this work and compared to the gravitational acceleration $g(r) = GM(r)/r^2$ (represented by a thick solid black line). Each panel corresponds to a different value of the inner logarithmic slope of the dark matter density profile. For our canonical model with $\alpha = 1$, $g(r) \approx 2\pi G \rho_s r_s = 1.3 \times 10^{-10} \text{ m s}^{-1}$ in the innermost regions, whereas in the general case described by equation (25) gravity scales as $g(r) \propto r^{1-\alpha}$ for $r \ll r_s$.

Depending on the model parameters, the acceleration caused by the electron–positron gas may be comparable to (or even higher than) the gravitational one in the central parts of the halo. For our canonical model (left-hand panel of Fig. 7), the pressure gradient is strong enough to overcome gravity for $E_0 < 1 \text{ GeV}$, and the radius at which both forces balance each other is of the order of 100 pc. The effect of dark matter annihilation is weaker, but perhaps still measurable, for $E_0 \sim 1 \text{ GeV}$. It would be extremely difficult to detect at 10 GeV, and completely negligible for larger particle masses. These conclusions are very robust with respect to variations in the ionization fraction of the gas or the intensity of the magnetic field. The exact density of the ISM has a somewhat larger influence on the results, partly because of its effect on the dark matter pressure (see Fig. 5) and partly through the presence of the gas density in equation (2). For the extreme case $E_0 = 100 \text{ MeV}$ and $\rho_g/m_p = 0.1 \text{ cm}^{-3}$, dark matter pressure is able to prevent gravitational collapse within the inner 2 kpc, compared to 100 pc for a density of 10 cm^{-3} . However, the qualitative picture is not changed. For $E_0 > 10 \text{ GeV}$, the gravitational acceleration dominates by several orders of magnitude at all radii, even for the most dilute gas.

As shown in the previous section, the logarithmic slope of the density profile plays a critical role on the pressure profile. The

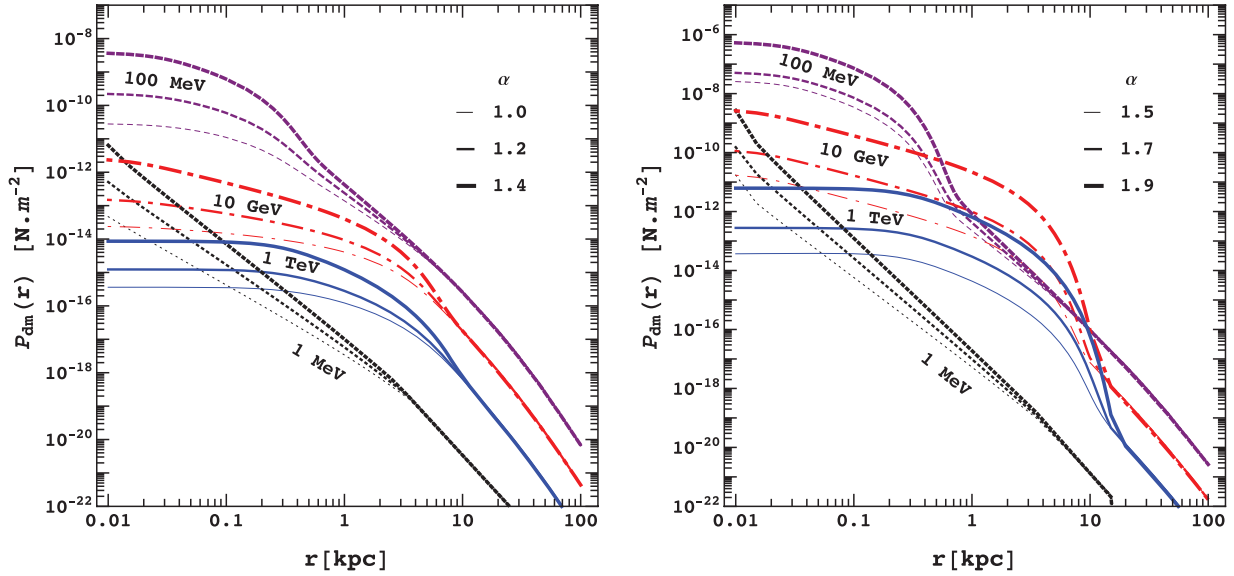


Figure 6. Dark matter pressure for different values of E_0 and the inner logarithmic slope α of the dark matter density profile.

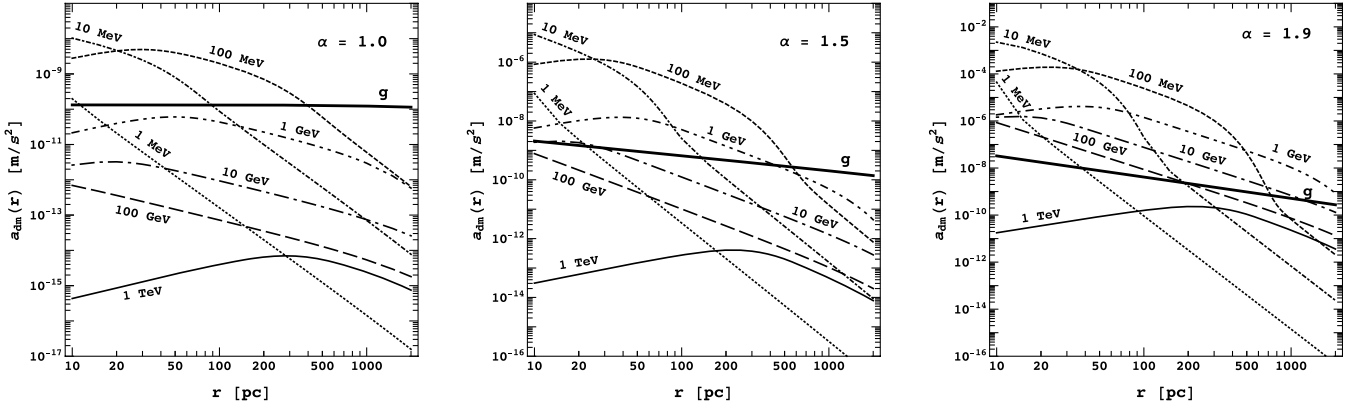


Figure 7. Dark matter acceleration for different values of the injection energy E_0 and the inner logarithmic slope α .

accelerations for $\alpha = 1.5$ and 1.9 are shown on the centre and right-hand panels of Fig. 7, respectively. When $\alpha = 1.9$, the radius at which the relativistic pressure balances gravity ranges from a few tens of pc up to several kpc, and a sizable effect on the rotation curve of the Galaxy is expected for any value of the injection energy $E_0 < 1$ TeV.

Fig. 8 shows the modified circular velocity profiles, according to expression (3), for different values of α and E_0 . In our canonical model, the rotation curve of the Galaxy changes significantly for $E_0 = 100$ MeV, it is slightly modified for $E_0 = 10$ MeV and almost imperceptibly for $E_0 = 1$ GeV. For higher values of the inner logarithmic slope, as those predicted, for instance, in the adiabatic contraction scenario (Blumenthal et al. 1986), it is more likely that the annihilation of dark matter particles leaves a clearly detectable imprint on the observed rotation curve. The scales on which such a signal would be visible, of the order of kpc in some cases, subtend several degrees on the sky for the Milky Way, and may be observable as well in other nearby galaxies.

In order to quantify the effect on the rotation curves of low surface brightness galaxies, we compute the model predictions for the objects compiled by de Blok & Bosma (2002). Since it is not our aim to fit the data (which would require more careful modelling, beyond the scope of the present work), we simply take the ob-

served rotation curves, as well as the quoted decomposition into stellar disc, gaseous disc and dark matter halo. We consider their constant mass-to-light ratio and maximum disc models, adopting the corresponding best-fitting values of V_{200} and c_{200} (table 4 in de Blok & Bosma 2002). Values of ρ_s and r_s for the maximum disc and constant mass-to-light ratio cases are given in Tables 3 and 4, respectively.

Fig. 9 shows the predicted rotation curves for $\gamma_0 = 200$ ($m_{\text{dm}}c^2 \sim 100$ MeV) and $\gamma_0 = 2000$ ($m_{\text{dm}}c^2 \sim 1$ GeV) with $\langle\sigma v\rangle_{e^\pm} = 2.6 \times 10^{-26} \text{ cm}^3 \text{ s}^{-1}$ and all other parameters set to our canonical values. Since these rotation curves have been computed (at least, in the innermost regions) from the H α line, we also plot the results obtained for a gas density $n = \rho_g/m_p = 0.01 \text{ cm}^{-3}$ and $x_{\text{ion}} = 1$, appropriate for the hot, diffuse component responsible for the emission line. The original model of de Blok & Bosma (2002) without dark matter annihilation is shown for the sake of comparison, and the reduced χ^2 values associated to each model are listed in Tables 3 and 4.

In general, the effect is not very significant for $n = 1 \text{ cm}^{-3}$ (not even for $m_{\text{dm}}c^2 \sim 100$ MeV, except for a few exceptional cases, such as NGC 3274). For the adopted value of the logarithmic slope of the dark matter density profile near the centre, $\alpha = 1$, and the extremely low values of the characteristic density ρ_s reported by

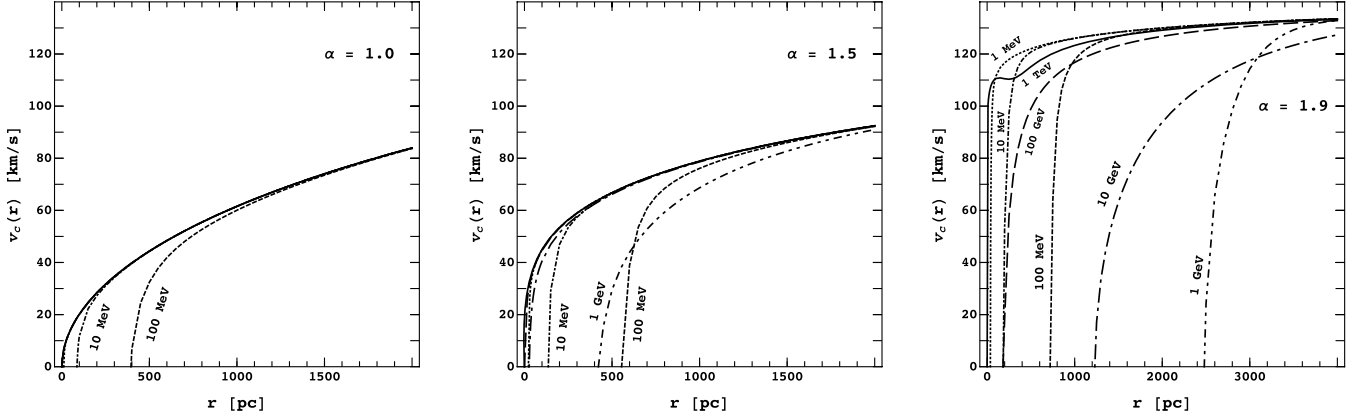


Figure 8. Effect of dark matter annihilation on the rotation curve. From left to right, panels correspond to $\alpha = 1.0$ (our canonical model), 1.5 and 1.9, respectively.

Table 3. Galaxy name, characteristic dark matter density and radius and reduced χ^2 values for the maximum disc models in de Blok & Bosma (2002). χ^2_{dBB} refers to the original model without dark matter annihilation. The subscripts in the other columns denote the injection energy (100 MeV or 1 GeV) and the conditions in the baryonic medium ($n = 1 \text{ cm}^{-3}$ and $x_{\text{ion}} = 0$ for H I, $n = 0.01 \text{ cm}^{-3}$ and $x_{\text{ion}} = 1$ for H II).

Name	$\rho_s c^2 \text{ (GeV cm}^{-3}\text{)}$	$r_s \text{ (kpc)}$	χ^2_{dBB}	$\chi^2_{100 \text{ MeV, H I}}$	$\chi^2_{1 \text{ GeV, H I}}$	$\chi^2_{100 \text{ MeV, H II}}$	$\chi^2_{1 \text{ GeV, H II}}$
UGC 1230	9.2799×10^{-2}	15.152	0.723	0.713	0.720	49.825	0.430
UGC 5005	8.5056×10^{-5}	4206.9	0.521	0.520	0.521	4.726	0.488
LSBC F563–01	4.5080×10^{-3}	188.61	0.383	0.381	0.383	27.368	0.345
UGC 4173	8.5056×10^{-5}	1765.8	0.225	0.225	0.225	1.223	0.214
UGC 3371	8.5056×10^{-5}	7302.7	0.387	0.383	0.386	17.775	0.273
NGC 1560	8.5056×10^{-5}	7131.5	8.914	9.183	8.896	659.459	8.720
DDO 189	3.9944×10^{-3}	135.71	0.173	0.171	0.173	40.124	0.135
NGC 4395	3.8588×10^{-1}	5.8478	0.573	1.627	0.555	743.952	14.954
NGC 3274	4.4477×10^{-1}	6.7189	1.787	7.139	1.731	2935.570	33.516
NGC 4455	8.5056×10^{-5}	8252.1	1.428	1.694	1.419	320.260	1.643
NGC 2366	1.7431×10^{-1}	2.3734	1.246	1.209	1.245	58.692	1.204
UGC 4325	8.5056×10^{-5}	23618	1.326	1.294	1.300	748.686	4.459
DDO 47	8.5056×10^{-5}	14107	0.400	0.303	0.394	260.841	2.056
DDO 185	8.5056×10^{-5}	5245.2	2.036	2.024	2.026	141.203	1.896

Table 4. Same as Table 3, but for the constant mass-to-light ratio models in de Blok & Bosma (2002).

Name	$\rho_s c^2 \text{ (GeV cm}^{-3}\text{)}$	$r_s \text{ (kpc)}$	χ^2_{dBB}	$\chi^2_{100 \text{ MeV, H I}}$	$\chi^2_{1 \text{ GeV, H I}}$	$\chi^2_{100 \text{ MeV, H II}}$	$\chi^2_{1 \text{ GeV, H II}}$
UGC 1230	3.7001×10^{-1}	9.0973	1.091	1.032	1.072	257.449	5.447
UGC 5005	9.1650×10^{-3}	75.759	0.175	0.172	0.174	18.571	0.102
LSBC F563–01	9.9553×10^{-2}	20.850	0.370	0.355	0.367	155.857	1.492
UGC 4173	8.5056×10^{-5}	2413.7	0.124	0.123	0.124	3.687	0.110
UGC 3371	8.5056×10^{-5}	10073	0.280	0.273	0.278	36.263	0.118
NGC 1560	5.6447×10^{-3}	166.59	2.330	3.810	2.315	1905.660	17.378
DDO 189	2.2759×10^{-3}	7.4629	0.109	0.088	0.105	273.964	5.120
NGC 4395	4.4477×10^{-1}	6.3057	0.644	2.476	0.613	1149.580	30.584
NGC 3274	2.2174×10^{-0}	2.9131	0.941	29.406	0.808	9205.720	371.555
NGC 4455	8.5056×10^{-5}	9702.7	0.614	1.078	0.605	466.972	2.482
NGC 2366	3.8588×10^{-1}	4.1902	1.935	2.222	1.900	950.701	16.488
UGC 4325	8.5056×10^{-5}	36371	1.096	1.081	1.047	1737.360	34.844
DDO 47	8.5056×10^{-5}	16137	0.272	0.180	0.265	344.709	3.186
DDO 185	8.5056×10^{-5}	7876.7	2.162	2.333	2.138	366.502	3.996

de Blok & Bosma (2002), the circular velocity at the innermost point becomes reduced by an amount that is typically much smaller than the observational error bars. A more noticeable effect would be obtained for steeper profiles (see Fig. 8), but also if one considers

the typical density of the hot, ionized medium where the H α line originates. Using $n = 0.01 \text{ cm}^{-3}$, the rotation curves of *all* galaxies would be dramatically affected on $\sim \text{kpc}$ scales for $\alpha = 1$ and $E_0 \leq \text{GeV}$, both for the constant M/L and maximum disc models.

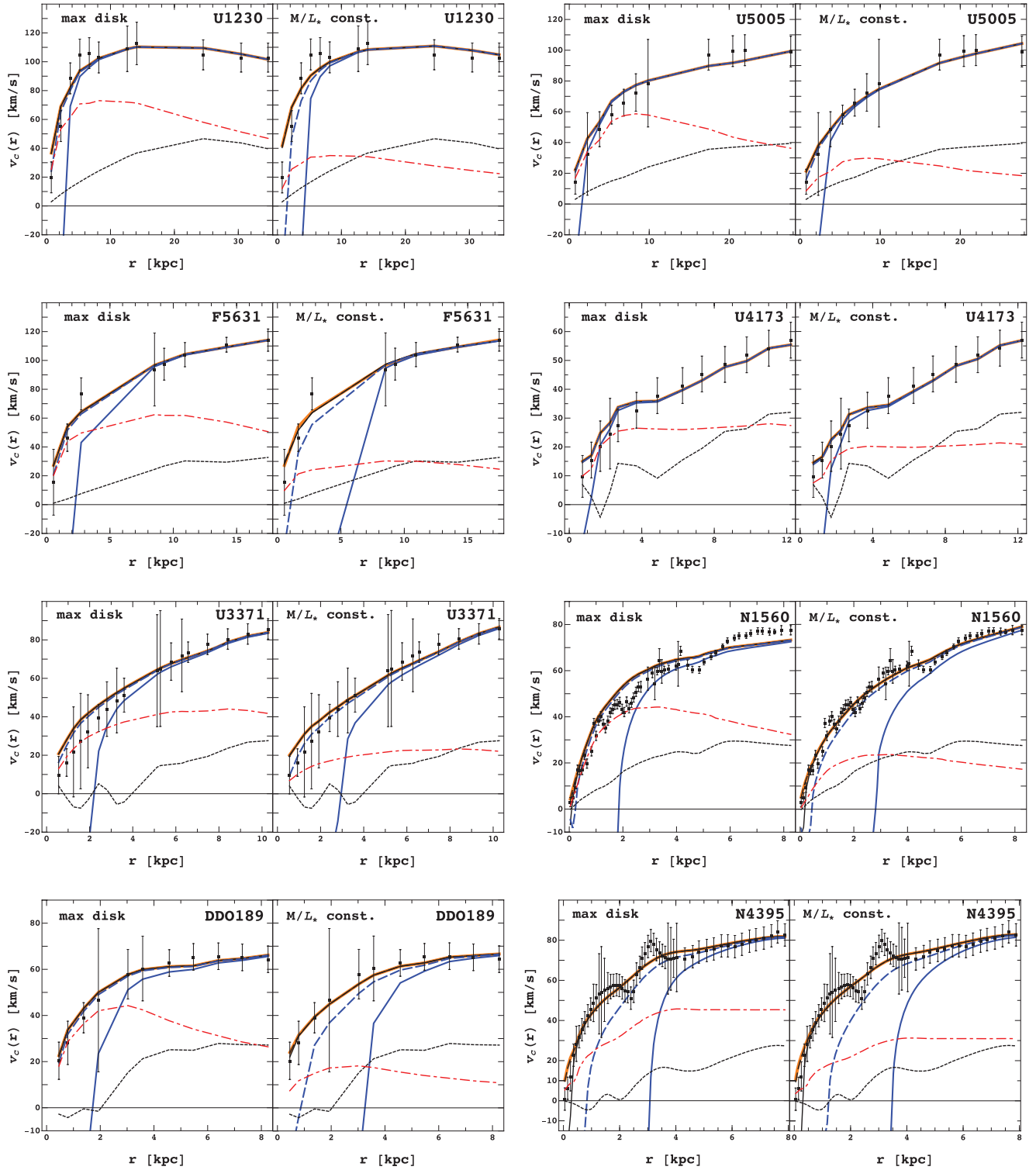


Figure 9. Model predictions, compared to the observed rotation curves (data points with error bars). Solid lines are used for $E_0 = 100$ MeV and dashed lines for 1 GeV. Results for neutral and ionized gas are shown in black and blue colour, respectively. Orange lines depict the model without dark matter annihilation. The rotation curves by star and gas (data taken from de Blok & Bosma 2002) are shown by red dot-dashed and black small dashed lines, respectively.

These results represent a double-edged sword for dark matter annihilation models. On the one hand, it might be possible to find a particular dark matter candidate that is able to explain the rotation curve data with a cuspy density profile. On the other hand, we also predict that, in that case, one should observe prominent differences

in the kinematics of the stellar, neutral and ionized components due to their different densities. The observed rotation curves provide thus an additional tool (complementary to radio and gamma-ray constraints) to rule out a broad class of models and hopefully help to identify the physical properties of dark matter particles.

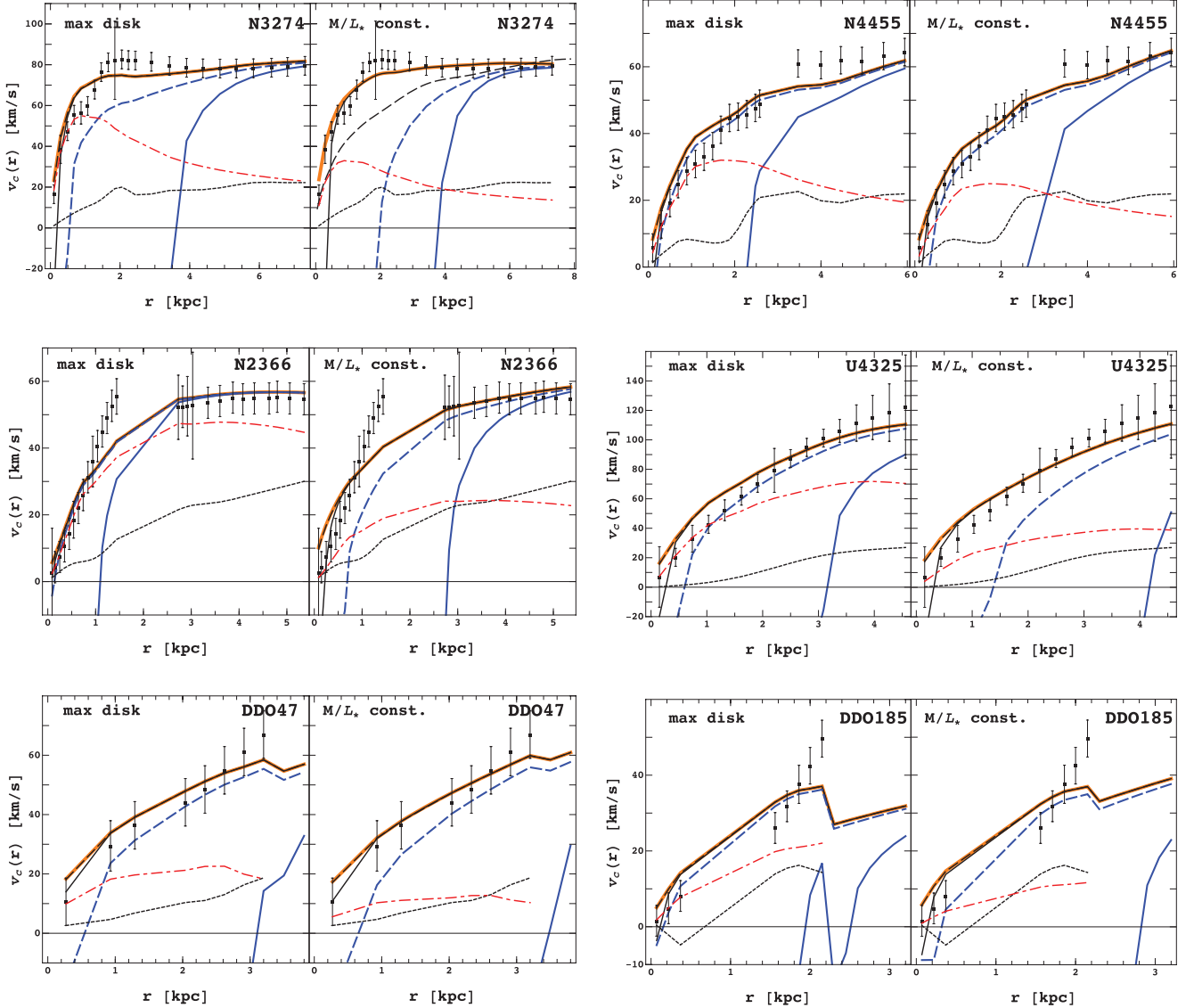


Figure 9 – continued

5 CONCLUSIONS

In this paper, we have investigated the contribution to the total gas pressure arising from relativistic electrons and positrons produced in dark matter annihilations. The propagation of these particles through the ISM is determined by the diffusion-loss equation. We assume a uniform diffusion coefficient and consider ICS, synchrotron radiation, Coulomb collisions, bremsstrahlung and ionization of neutral hydrogen atoms as the main energy loss mechanisms. All the electrons and positrons are injected with an initial energy E_0 between 1 MeV and 1 TeV, and the injection rate is constrained by different Galactic observations.

We have evaluated the effect of this ‘dark matter pressure’ for astrophysical conditions representative of the Milky Way and varied the adopted values of each parameter (intensity of the magnetic field, density and ionization fraction of the ISM gas, inner logarithmic slope of the dark matter density profile and the virial mass of the galaxy) to verify that our results hold in the general case. Our main conclusions can be summarized as follows.

(i) For the canonical Milky Way model, the dark matter pressure gradient is able to offset the gravitational acceleration within the central $\sim 10\text{--}400$ pc as long as the injection energy is lower than 1 GeV. There would be an extremely weak signature if $E_0 \sim \text{GeV}$, and the effect would be completely negligible for larger values of E_0 .

(ii) The ionization fraction of the ISM and the intensity of the magnetic field determine the energy losses and the shape of the electron–positron spectrum at low and high values of the Lorentz factor, respectively. Although these details may have a strong impact on other observables, such as the emission at different wavelengths, they do not affect the rotation curve significantly. The precise value of the gas density plays a more important role, and it changes the results at the quantitative level.

(iii) Steep logarithmic slopes of the dark matter density profile yield much higher pressures in the central regions. For $\alpha \geq 1.9$, a clear signature of dark matter annihilation on the observed rotation curve is expected even for $E_0 \sim 1$ TeV.

(iv) Comparison with publicly available observational data shows that, while dark matter pressure may bring the predicted

rotation curves into better agreement with observations, it is arguably more likely that this effect is more useful as a constraint on the annihilation cross-section as a function of dark matter particle mass.

ACKNOWLEDGMENTS

MW would like to thank V. Müller and the members of the cosmology group at the AIP for useful discussions, as well as F. Breitling for his help with programming questions and S. White for English corrections. This work has been funded by DFG Research Grant AS 312/1-1 (Germany). YA also acknowledges support from project AYA 2007-67965-C03-03 (MEC, Spain). The authors would also like to thank the referee for a very helpful report.

REFERENCES

- Abdo A. A. [Fermi collaboration] et al., 2009, *Phys. Rev. Lett.*, 102, 181101
- Adriani O. [PAMELA collaboration] et al., 2009a, *Nat*, 458, 607
- Adriani O. [PAMELA collaboration] et al., 2009b, *Phys. Rev. Lett.*, 102, 051101
- Aharonian F. [HESS collaboration] et al., 2006, *Phys. Rev. Lett.*, 97, 221102
- Aharonian F. [HESS collaboration] et al., 2008, *Phys. Rev. Lett.*, 101, 261104
- Ascasibar Y., 2007, *A&A*, 462, L65
- Ascasibar Y., Díaz A. I., 2010, *MNRAS*, 404, 275
- Ascasibar Y., Gottlöber S., 2008, *MNRAS*, 386, 2022
- Ascasibar Y., Yepes G., Gottlöber S., Müller V., 2004, *MNRAS*, 352, 1109
- Ascasibar Y., Jean P., Böhm C., Knödseder J., 2006, *MNRAS*, 368, 1695
- Baltz E. A., Edsjö J., 1999, *Phys. Rev. D*, 59, 023511
- Beck R., 2001, *Space Sci. Rev.*, 99, 243
- Bergström L., Ullio P., Buckley J. H., 1998, *Astropart. Phys.*, 9, 137
- Bergström L., Bertone G., Bringmann T., Edsjö J., Taoso M., 2009, *Phys. Rev. D*, 79, 081303
- Bernal N., Palomares-Ruiz S., 2010, preprint (arXiv:1006.0477)
- Bertone G., Hooper D., Silk J., 2005, *Phys. Rep.*, 405, 279
- Blumenthal G. R., Gould R. J., 1970, *Rev. Modern Phys.*, 42, 237
- Blumenthal G. R., Faber S. M., Flores R., Primack J. R., 1986, *ApJ*, 301, 27
- Borriello A., Salucci P., 2001, *MNRAS*, 323, 285
- Burkert A., 1995, *ApJ*, 447, L25
- Cen R., 2001, *ApJ*, 546, L77
- Cesarini A., Fucito F., Lionetto A., Morselli A., Ullio P., 2004, *Astropart. Phys.*, 21, 267
- Chen X., Kamionkowski M., 2004, *Phys. Rev. D*, 70, 043502
- Cholis I., Goodenough L., Hooper D., Simet M., Weiner N., 2009, *Phys. Rev. D*, 80, 123511
- Chuzhoy L., 2008, *ApJ*, 679, L65
- Cirelli M., Panci P., 2009, *Nuclear Phys. B*, 821, 399
- Cirelli M., Iocco F., Panci P., 2009, *J. Cosmol. Astropart. Phys.*, 10, 9
- Colafrancesco S., 2004, *A&A*, 422, L23
- Colafrancesco S., Mele B., 2001, *ApJ*, 562, 24
- Colín P., Avila Reese V., Valenzuela O., 2000, *ApJ*, 542, 622
- Crocker R. M., Bell N. F., Balázs C., Jones D. I., 2010, *Phys. Rev. D*, 81, 063516
- Cumberbatch D. T., Zuntz J., Kamfjör Eriksen H. K., Silk J., 2009, preprint (arXiv:0902.0039)
- Davé R., Spergel D. N., Steinhardt P. J., Wandelt B. D., 2001, *ApJ*, 547, 574
- de Blok W. J. G., 2010, *Advances Astron.*, doi:10.1155/2010/789293
- de Blok W. J. G., Bosma A., 2002, *A&A*, 385, 816
- de Blok W. J. G., McGaugh S. S., Bosma A., Rubin V. C., 2001, *ApJ*, 552, L23
- de Blok W. J. G., Walter F., Brinks E., Trachternach C., Oh S., Kennicutt R. C., 2008, *AJ*, 136, 2648
- Dehnen W., Binney J., 1998, *MNRAS*, 294, 429
- Delahaye T., Lineros R., Donato F., Fornengo N., Lavalley J., Salati P., Taillet R., 2009, *A&A*, 501, 821
- Diemand J., Zemp M., Moore B., Stadel J., Carollo C. M., 2005, *MNRAS*, 364, 665
- Diemand J., Kuhlen M., Madau P., Zemp M., Moore B., Potter D., Stadel J., 2008, *Nat*, 454, 735
- Donato F., Fornengo N., Maurin D., Salati P., Taillet R., 2004a, *Phys. Rev. D*, 69, 063501
- Donato F., Gentile G., Salucci P., 2004b, *MNRAS*, 353, L17
- Dubinski J., Carlberg R. G., 1991, *ApJ*, 378, 496
- El-Zant A., Shlosman I., Hoffman Y., 2001, *ApJ*, 560, 636
- Ferrière K. M., 2001, *Rev. Modern Phys.*, 73, 1031
- Flores R. A., Primack J. R., 1994, *ApJ*, 427, L1
- Fornasa M., Pieri L., Bertone G., Branchini E., 2009, *Phys. Rev. D*, 80, 023518
- Fukushige T., Makino J., 1997, *ApJ*, 477, L9
- Fukushige T., Makino J., 2001, *ApJ*, 557, 533
- Fukushige T., Kawai A., Makino J., 2004, *ApJ*, 606, 625
- Furlanetto S. R., Oh S. P., Pierpaoli E., 2006, *Phys. Rev. D*, 74, 103502
- Galli S., Iocco F., Bertone G., Melchiorri A., 2009, *Phys. Rev. D*, 80, 023505
- Gao L., Navarro J. F., Cole S., Frenk C. S., White S. D. M., Springel V., Jenkins A., Neto A. F., 2008, *MNRAS*, 387, 536
- Gentile G., Salucci P., Klein U., Vergani D., Kalberla P., 2004, *MNRAS*, 351, 903
- Gentile G., Famaey B., de Blok W. J. G., 2011, *A&A*, 527, A76
- Ghigna S., Moore B., Governato F., Lake G., Quinn T., Stadel J., 1998, *MNRAS*, 300, 146
- Ghigna S., Moore B., Governato F., Lake G., Quinn T., Stadel J., 2000, *ApJ*, 544, 616
- Gondolo P., Silk J., 1999, *Phys. Rev. Lett.*, 83, 1719
- Goodman J., 2000, *Nat*, 5, 103
- Hayashi E. et al., 2004, *MNRAS*, 355, 794
- Hooper D., Finkbeiner D. P., Dobler G., 2007, *Phys. Rev. D*, 76, 083012
- Hu W., Barkana R., Gruzinov A., 2000, *Phys. Rev. Lett.*, 85, 1158
- Iocco F., Bressan A., Ripamonti E., Schneider R., Ferrara A., Marigo P., 2008, *MNRAS*, 390, 1655
- Jing Y. P., Suto Y., 2000, *ApJ*, 529, L69
- Kanzaki T., Kawasaki M., Nakayama K., 2010, *Progress Theor. Phys.*, 123, 853
- Kaplinghat M., Knox L., Turner M. S., 2000, *Phys. Rev. Lett.*, 85, 3335
- Klypin A., Kravtsov A. V., Bullock J. S., Primack J. R., 2001, *ApJ*, 554, 903
- Klypin A., Zhao H., Somerville R. S., 2002, *ApJ*, 573, 597
- Kravtsov A. V., Klypin A. A., Bullock J. S., Primack J. R., 1998, *ApJ*, 502, 48
- Kuzio de Naray R., McGaugh S. S., de Blok W. J. G., 2008, *ApJ*, 676, 920
- Longair M. S., 1981, *High Energy Astrophysics: An Informal Introduction for Students of Physics and Astronomy*. Cambridge Univ. Press, Cambridge
- McGaugh S. S., de Blok W. J. G., 1998, *ApJ*, 499, 41
- Mapelli M., Ferrara A., Pierpaoli E., 2006, *MNRAS*, 369, 1719
- Marchesini D., D'Onghia E., Chincarini G., Firmani C., Conconi P., Molinari E., Zacchei A., 2002, *ApJ*, 575, 801
- Mashchenko S., Couchman H. M. P., Wadsley J., 2006, *Nat*, 442, 539
- Moore B., 1994, *Nat*, 370, 629
- Moore B., Governato F., Quinn T., Stadel J., Lake G., 1998, *ApJ*, 499, L5
- Moore B., Quinn T., Governato F., Stadel J., Lake G., 1999, *MNRAS*, 310, 1147
- Morselli A., Lionetto A., Cesarini A., Fucito F., Ullio P., 2002, *Nuclear Phys. B Proc. Suppl.*, 113, 213
- Natarajan P., Croton D., Bertone G., 2008, *MNRAS*, 388, 1652
- Natarajan A., Tan J. C., O'Shea B. W., 2009, *ApJ*, 692, 574
- Navarro J. F., Frenk C. S., White S. D. M., 1996, *ApJ*, 462, 563
- Navarro J. F., Frenk C. S., White S. D. M., 1997, *ApJ*, 490, 493
- Navarro J. F. et al., 2004, *MNRAS*, 349, 1039
- Navarro J. F. et al., 2010, *MNRAS*, 402, 21
- Oh S., de Blok W. J. G., Brinks E., Walter F., Kennicutt R. C., Jr, 2010a, *AJ*, (arXiv:1011.0899)
- Oh S., Brook C., Governato F., Brinks E., Mayer L., de Blok W. J. G., Brooks A., Walter F., 2010b, *AJ*, (arXiv:1011.2777)

- Padmanabhan N., Finkbeiner D. P., 2005, *Phys. Rev. D*, 72, 023508
- Pato M., Pieri L., Bertone G., 2009, *Phys. Rev. D*, 80, 103510
- Peebles P. J. E., 2000, *ApJ*, 534, L127
- Porter T. A., Strong A. W., 2005, in Acharya B. S., Gupta S., Jagadeesan P., Jain A., Karthikeyan S., Morris S., Tonwar S., eds, *Int. Cosmic Ray Conf. Vol. 4, A New Estimate of the Galactic Interstellar Radiation Field Between 0.1 μm and 1000 μm* . Tata Institute of Fundamental Research, Mumbai, p. 77
- Power C., Navarro J. F., Jenkins A., Frenk C. S., White S. D. M., Springel V., Stadel J., Quinn T., 2003, *MNRAS*, 338, 14
- Prada F., Klypin A., Flix J., Martínez M., Simonneau E., 2004, *Phys. Rev. Lett.*, 93, 241301
- Profumo S., Ullio P., 2010, preprint (arXiv:1001.4086)
- Reed D., Governato F., Verde L., Gardner J., Quinn T., Stadel J., Merritt D., Lake G., 2005, *MNRAS*, 357, 82
- Regis M., 2008, *Phys. Lett. B*, 663, 250
- Regis M., Ullio P., 2008, *Phys. Rev. D*, 78, 043505
- Rephaeli Y., 1979, *ApJ*, 227, 364
- Ripamonti E., Mapelli M., Ferrara A., 2007, *MNRAS*, 375, 1399
- Ripamonti E., Iocco F., Ferrara A., Schneider R., Bressan A., Marigo P., 2010, *MNRAS*, 406, 2605
- Robin A. C., Reylé C., Derrière S., Picaud S., 2003, *A&A*, 409, 523
- Sanders R. H., McGaugh S. S., 2002, *ARA&A*, 40, 263
- Sarazin C. L., 1999, *ApJ*, 520, 529
- Sofue Y., Rubin V., 2001, *ARA&A*, 39, 137
- Sommer-Larsen J., Dolgov A., 2001, *ApJ*, 551, 608
- Spano M., Marcelin M., Amram P., Carignan C., Epinat B., Hernandez O., 2008, *MNRAS*, 383, 297
- Spergel D. N., Steinhardt P. J., 2000, *Phys. Rev. Lett.*, 84, 3760
- Spolyar D., Freese K., Gondolo P., 2008, *Phys. Rev. Lett.*, 100, 051101
- Springel V. et al., 2008, *Nat*, 456, 73
- Stoeckl F., White S. D. M., Springel V., Tormen G., Yoshida N., 2003, *MNRAS*, 345, 1313
- Ullio P., Bergström L., Edsjö J., Lacey C., 2002, *Phys. Rev. D*, 66, 123502
- Valdés M., Ferrara A., Mapelli M., Ripamonti E., 2007, *MNRAS*, 377, 245
- Yoshida N., Springel V., White S. D. M., Tormen G., 2000, *ApJ*, 544, L87
- Zhang L., Chen X., Lei Y., Si Z., 2006, *Phys. Rev. D*, 74, 103519
- Zhang L., Chen X., Kamionkowski M., Si Z., Zheng Z., 2007, *Phys. Rev. D*, 76, 061301

This paper has been typeset from a \LaTeX file prepared by the author.